Journal of
Materials Chemistry C

COMMUNICATION

View Article Online
View Journal | View Issue

Cite this: J. Mater. Chem. C, 2016, 4, 1769

Received 25th November 2015,
Accepted 8th February 2016

DOI: 10.1039/c5tc03970c

www.rsc.org/MaterialsC

Calculation of dopant solubilities and phase diagrams of X–Pb–Se (X = Br, Na) limited to defects with localized charge

Saurabh Bajaj,[ab] Heng Wang,[a] Jeff W. Doak,[c] Chris Wolverton[c] and G. Jeffrey Snyder*[ac]

The control of defects, particularly impurities, to tune the concentrations of electrons and holes is of utmost importance in the use of semiconductor materials. To estimate the amount of dopant that can be added to a semiconductor without precipitating secondary phases, a detailed phase diagram is needed. The ability of *ab initio* computational methods to predict defect stability can greatly accelerate the discovery of new semiconductors by calculating phase diagrams when time-consuming experimental ones are not available. DFT defect energy calculations are particularly successful in identifying doping strategies by determining the energy of multiple defect charge states in large band gap semiconductors and insulators. In metals, detailed phase diagrams can be determined from such calculations but only one, uncharged defect is needed. In this work, we have calculated dopant solubilities of Br and Na in the thermoelectric material PbSe by mapping its solvus boundaries in different regions of the respective ternary phase diagrams using DFT defect energy calculations. The narrow gap PbSe provides an example where defects with nominal charge state (based on valence counting) have properly-localized charge states. However, defects with unexpected charge states produce delocalized electrons, which are then, in effect, defects with the expected charge state. Simply applying the methods for calculating multiple defect charge states in PbSe and treating them as separate defects fails to predict properties measured by experiments. Performing thermodynamic calculations using only the expected charge states, excluding others, enables accurate prediction of experimentally measured doping efficiencies and phase diagrams. Identifying which defect charge states to include in thermodynamic calculations will expedite the use of such calculations for other semiconductors in understanding phase diagrams and devising effective doping strategies.

1. Introduction

Impurity dopants are key to unlocking the potential of semiconductors for a variety of applications. Impurities act as extrinsic dopants that allow for precise control over charge carrier sign and densities. In a semiconductor with an ideal dopant, the excess charge supplied is directly related to the dopant concentration. In PbSe, for example, the substitution of a Br atom for a Se atom should make an ideal n-type dopant because each Br brings one extra electron even though the electronic states of Br are essentially the same as those of Se. Similarly the substitution of Na for Pb should be ideal for p-type PbSe. In many applications, the performance of a semiconductor is limited by the dopant solubility, which is the amount of dopant that can be incorporated[1] before a dopant-rich secondary phase precipitates from the semiconductor (known as dopant precipitation). Such formation and evolution of unwanted secondary phases often harms lifetime performance, or even the stability and integrity of the material. A phase diagram provides essential information for material design to address these challenges. However, experimental phase diagrams are not always available, or available without enough detail in the region of interest. In such cases, calculated phase diagrams could provide alternative guidelines and help in the development new materials.

Density functional theory (DFT)[2,3] based defect energy calculations provide powerful insights for understanding properties of lightly doped semiconductors used as photovoltaics or optoelectronics (see, for example ref. 4) that have band gaps of nearly 1 eV or greater. Such studies have been particularly helpful in identifying charge state transitions of deep defects, states that form well inside the forbidden energy gap.

In this study, we use DFT methods to investigate the defect thermodynamics of ideal dopants in the narrow band gap ($\approx$0.3 eV) semiconductor PbSe. Experiments performed for this work show that Br is indeed an ideal donor dopant and Na is an ideal acceptor dopant with essentially 100% doping effectiveness, indicating that one charge carrier is measured for each impurity atom. Doping effectiveness is defined as the ratio of

[a] Department of Applied Physics and Materials Science, California Institute of Technology, Pasadena, CA 91125, USA
[b] Environmental Energy Technologies Division, Lawrence Berkeley National Laboratory, Berkeley, California 94720, USA
[c] Department of Materials Science and Engineering, Northwestern University, Evanston, IL 60208, USA. E-mail: jeff.snyder@northwestern.edu

carrier concentration of the sample to the amount of dopant added to it and is given by,

$$\eta = \frac{n-p}{\sum_{d,q} c_{d,q}'} \text{ or } \frac{p-n}{\sum_{d,q} c_{d,q}'}, \quad (1)$$

where the numerator is electron concentration $(n - p)$ in the case of Br–Pb–Se and $(p - n)$ in the case of Na–Pb–Se, and $\sum_{d,q} c_{d,q}'$ is the total atom concentration of the dopant in the PbSe phase found by summing over all the dopant containing defects. PbSe is chosen because the lead chalcogenides (PbQ, Q = Te, Se, S) with the rock-salt structure are excellent thermoelectric materials[5–13] for applications between 600 K and 900 K,[14] where its zT exceeds 1[13] for both p-type[6] and n-type[8] materials. Br is chosen due to its comparable size and electronic structure to Se, and reported $zT = 1.1 \pm 0.1$ at 850 K.[8] Similarly, Na provides fine control over hole carrier concentration[5,15] that leads to zT close to 1 at 850 K in PbSe.[6,16]

Despite the frequent use of these impurity dopants, no experimental literature is available (to the authors knowledge) on the phase diagrams of Br–Pb–Se or Na–Pb–Se, which is unsurprising due to the complexity of the experiments required to determine a ternary phase diagram. Accurate calculations of dopant solubilities could supplant tiresome experiments in the search for new semiconductors.

2. Methodology

The solubility limits of dopants in the PbSe phase in the ternary phase spaces of the Br–Pb–Se and Na–Pb–Se systems are determined by first using DFT[17] to calculate the defect formation energies of intrinsic and extrinsic defects consisting of vacancies (V_{Pb}, V_{Se}), substitutions (Pb_{Se}, Se_{Pb}), interstitials (Pb_i, Se_i), and dopant-containing defects consisting of Br and Na substitutions on Pb or Se (Br_{Pb}, Br_{Se}, Na_{Pb}, Na_{Se}), as well as interstitial Br and Na (Br_i, Na_i), all in neutral and charged states ranging from −2 to +2. The defect formation energy of a defect d of charge q is given by,[18]

$$\Delta E_{d,q} = [E_{d,q} - E_H] + \sum_\alpha n_\alpha^d(\mu_\alpha^0 + \Delta\mu_\alpha) + q(E_{VBM} + \Delta V_{PA} + \mu_e) + \Delta E_{IC}, \quad (2)$$

where $E_{d,q}$ and E_H are the DFT total energies of the defect containing PbSe supercell and the pure PbSe supercell, respectively, n_α^d is the number of atoms added ($n_\alpha^d = -1$) or removed ($n_\alpha^d = +1$) from the pure supercell to form the defect, μ_α^0 is the chemical potential of element α in its ground state or standard metallic state, and $\Delta\mu_\alpha$ is the change in the chemical potential of α corresponding to a particular phase equilibrium between PbSe and other compounds in the X–Pb–Se systems. μ_α^0 and $\Delta\mu_\alpha$ are calculated using elemental ground state energies and compound formation energies taken from the Materials Project[19–21] (the calculation settings used by the Materials Project are verified to be the same as those used in the calculation of defect energies in this work so as to avoid any errors in the formation energies). E_{VBM} is the energy of the valence band maximum (VBM) and corresponds to the energy of the highest occupied level. ΔV_{PA} is the potential alignment (PA) correction term used to re-align defect energy levels with energy levels of the host supercell, and is calculated using $\Delta V_{PA} = \left(\overline{V_{d,q}^r - V_H^r}\right)$,[22] where $V_{d,q}^r$ and V_H^r are the spherically-averaged electrostatic potentials of the defect and host supercells, respectively, far from the defect site so as to avoid including any spurious chemical interactions with it. The potential alignment correction term ranges from +0.08 eV to −0.13 eV for various charged defects. ΔE_{IC} is the image charge correction energy term that is added to the defect formation energy in order to model a true isolated charge defect in a size-limited supercell in non-degenerate conditions, and is calculated using the Makov–Payne expansion.[23] The dielectric constant ε used in this expansion is calculated to be equal to 594 (including both ion-clamped and ionic contributions) for PbSe using density functional perturbation theory as implemented in the Vienna Ab-initio Simulation Package (VASP).[24–26] Due to the high dielectric constant of PbSe, ΔE_{IC} has a maximum value of $\approx$7 meV in this work for $q \pm 2$ charges, and thus has a minimal effect on defect formation energies. Finally, μ_e in eqn (2) is the electron chemical potential that is the additional energy of electrons in our system, and is set to range in values around the energies of the VBM and CBM (conduction band minimum) for plots showing the variation of defect formation energies as functions of electron chemical potential. μ_e is calculated as a function of temperature T and chemical potentials $\{\mu_\alpha\}$ by solving the charge-neutrality condition,

$$n - p = \sum_d q_d c_{d,q}, \quad (3)$$

where n and p are the free carrier concentrations of electrons and holes given by,[27]

$$n = \int_{E_{CBM}}^{+\infty} n(E) f(E;\mu_e,T)\mathrm{d}E, \qquad p = \int_{-\infty}^{E_{VBM}} n(E)[1 - f(E;\mu_e,T)]\mathrm{d}E, \quad (4)$$

where $n(E)$ is the density of states of the defect-free crystal, and $f(E;\ \mu_e,T)$ is the Fermi–Dirac distribution. $c_{d,q}$ is the defect concentration, and in the dilute limit is given by,[27]

$$c_{d,q} = N_{site}^{d,q} N_{sym}^{d,q} e^{-\Delta E_{d,q}/kT}, \quad (5)$$

where $N_{site}^{d,q}$ is the number of defect sites per formula unit of PbSe and $N_{sym}^{d,q}$ is the number of geometrically distinct but symmetrically equivalent ways of adding defect d with charge state q to a site.

The solvus boundaries of PbSe in the X–Pb–Se systems are calculated by summing over concentrations of each defect d, weighted by $-n_\alpha^d$, which is the change in composition of the XPbSe phase due to that defect, and is given by,[28]

$$n_\alpha = \sum_d -n_\alpha^d c_{d,q}. \quad (6)$$

When calculated under chemical potentials $\{\mu_\alpha\}$, which represent different phase equilibrium regions between PbSe and other compounds in the phase diagram, and at a particular temperature T, we obtain an isothermal section of the phase boundaries of PbSe in the system X–Pb–Se. Further details of this methodology can be found in ref. 29.

3. Results and discussion

Fig. 1 and 2 show the defect formation energies of the lowest energy defects in the Br–Pb–Se and Na–Pb–Se systems, respectively, plotted as a function of electron chemical potential or Fermi level μ_e for different regions of three-phase equilibrium that contain the PbSe phase. The dominant defects (defects with highest concentrations) of a system are determined by the equilibrium μ_e calculated as a function of temperature and atomic chemical potentials by numerically solving the charge neutrality condition in eqn (3). In the case of Br–Pb–Se, the equilibrium μ_e is positioned where, from Fig. 1, the lowest energy defects are Br_{Se}^{+1} and V_{Pb}^{-2} in the Se-rich PbSe–Se–$PbBr_2$ region and Br_{Se}^{+1} and Br_{Se}^{0} in the Pb-rich Pb–PbSe–$PbBr_2$ region. In Na–Pb–Se, from Fig. 2, the defect energy landscape in three out of the four regions of three-phase equilibria is dominated by the Na_{Pb}^{+2}, Na_{Pb}^{+1}, Na_{Pb}^{0}, and Na_{Pb}^{-1} defects. Whereas Na_{Pb}^{-1} is an acceptor defect that tends to dope PbSe p-type, the Na_{Pb}^{+2} and Na_{Pb}^{+1} defects are donor defects that tend to dope PbSe n-type. However, it is well-known

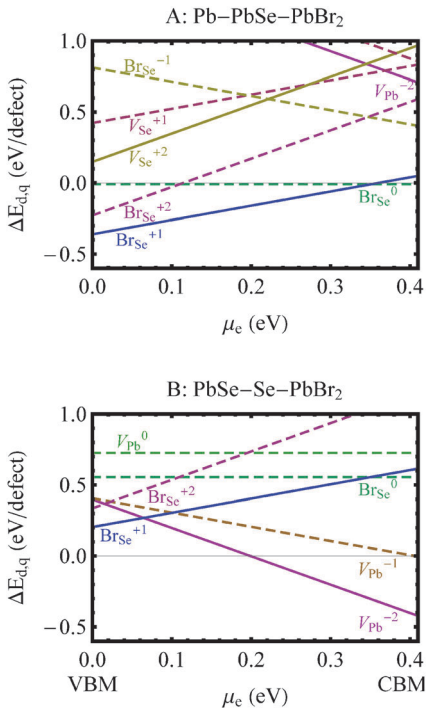

Fig. 1 Defect formation energies, $\Delta E_{d,q}$ of the lowest energy intrinsic and Br-containing defects in PbSe as a function of Fermi level, μ_e (relative to VBM) in different three phase equilibrium regions of PbSe in the Br–Pb–Se phase diagram. Solid lines indicate defects included in the calculation of the Br–Pb–Se phase diagram, whereas dashed lines indicate excluded defects.

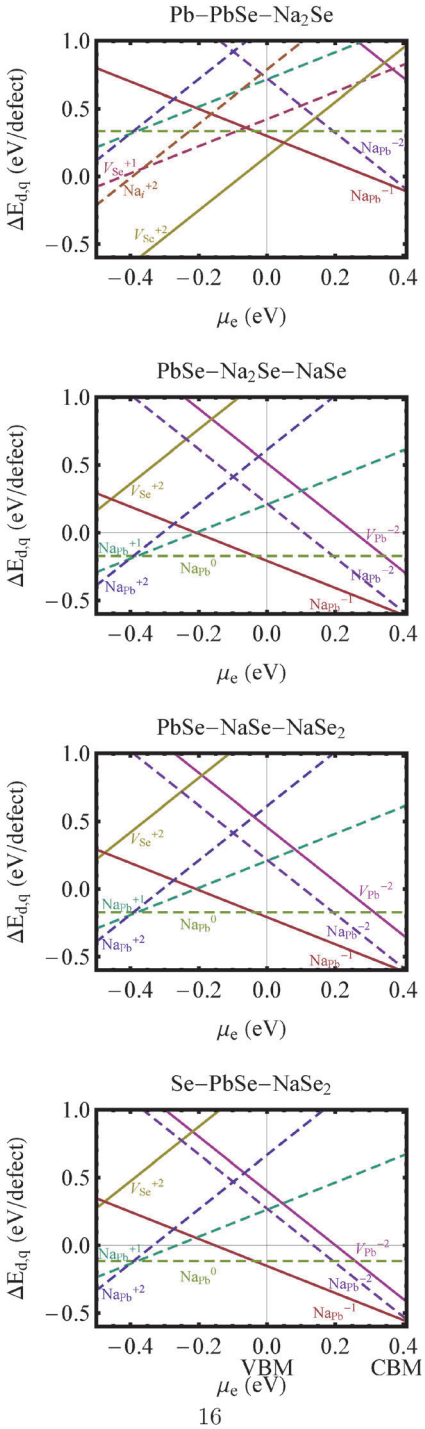

Fig. 2 Defect formation energies, $\Delta E_{d,q}$ of the lowest energy intrinsic and Na-containing defects in PbSe as a function of Fermi level, μ_e (relative to VBM) in different three phase equilibrium regions of PbSe in the Na–Pb–Se phase diagram. Solid lines indicate defects included in the calculation of the Na–Pb–Se phase diagram, whereas dashed lines indicate excluded defects.

that Na is a p-type dopant in PbQ systems[5,6,8,9,14,30,31] with Na substitution on the Pb^{+2} sublattice producing one conducting hole for each substitution. Thus, the Na_{Pb}^{+2} and Na_{Pb}^{+1} defects would not be expected to be present in notable concentrations, and this discrepancy will be addressed below. The unexpected

acceptor defects Br_{Se}^{-1} and Br_{Se}^{-2} do not pose an immediate problem as they are higher in energy than the defects shown in Fig. 1.

The remaining neutral defects, Br_{Se}^{0} in Br–Pb–Se and Na_{Pb}^{0} in Na–Pb–Se, would, according to the low energies calculated, appear to play a dominant role in determining the dopant concentrations and effectiveness. The formation energy of the Br_{Se}^{0} defect in the Pb-rich Pb–PbSe–$PbBr_2$ region is slightly negative at about −8.8 meV (independent of Fermi level), and the equilibrium Fermi level in these conditions is positioned where the formation energies of these defects are negative. A similar issue is seen in Na–Pb–Se (Fig. 2): the defect formation energy of Na_{Pb}^{0} is negative, with a minimum of −0.171 eV, in three out of four regions of three-phase equilibria: PbSe–Na_2Se–NaSe, PbSe–NaSe–$NaSe_2$, and Se–PbSe–$NaSe_2$. This issue is however not seen in the Na–Pb–Te system in which, from ref. 28, the Na_{Pb}^{0} defect is higher in energy and lower in concentration than the Na_{Pb}^{-1} defect at equilibrium Fermi levels in all regions of the phase diagram. Negative defect formation energies (of neutral defects, which do not depend on μ_e) lead to unusually large concentrations of defects, and thus low (essentially zero) dopant effectivity. If true, such defect formation energies would indicate non-equilibrium conditions or disorder at 0 K, and that the system could lower its energy by evolving to a different state with an ordered arrangement of these defects. There are several frequently suspected causes for negative defect formation energies, which are listed below. For each of them we provide a rational argument for its insufficient impact on the results,

– First, unknown ternary compounds in the Br–Pb–Se and Na–Pb–Se systems could change the chemical potential map and hence the defect energies:

The relative energy difference between defects of the same element type but different charge state (*e.g.*, Br_{Se}^{+1} *vs.* Br_{Se}^{0}) does not depend on the chemical potential. Thus the low doping effectiveness calculated due to neutral defects will not be affected by the presence of unknown ternary phases (discussed in more detail later in this section).

– Second, inaccuracy of correction methods, such as image charge, potential alignment, band-filling corrections (not included here):

Because the image charge and potential alignment corrections terms only affect charged defects, they cannot influence the neutral Br_{Se}^{0} and Na_{Pb}^{0} defects ($q = 0$ in eqn (2)). Additionally, the magnitude of band-filling corrections[32] are not expected to be significant enough to resolve the issues discussed here.

– Third, non-convergence of formation energies at employed supercell size:

The formation energies of the defects in question appear to be converged within 0.1 eV, while, as we shall see below, the defect energies are at least 0.5 eV too low. Furthermore, in this work, these energies are found to decrease with an increasing supercell size, which follows a trend opposite to what may resolve the issue of unexpectedly low formation energies.

– Fourth, as evidenced by an incorrect band gap, an incorrect determination of defect energies due to the DFT method employed that does not include spin–orbit coupling (SOC) effects, the use of hybrid functionals, or employment of the GW approach, *etc.*:

The calculated direct band gap of 0.41 eV at the *L* point using GGA over-estimates but is in fairly good agreement with the experimentally obtained value of 0.28 eV at room temperature.[33–35] Previous calculations in ref. 36–38 show that including SOC effects reduces the gap to near zero or negative values, representative of a metal, whereas the GW method or the use of hybrid HSE03 functionals, with and without SOC, leads to band gaps of ≈0.13 eV and 0.58 eV, respectively, which are both farther from experimental measurements than PBE-GGA. Also note that even in cases of materials with better agreement between calculated and experimental band gaps, the employment of these methods to defect supercells of size in the order used in this work (250 atoms) is computationally impractical. Although such calculations are plausible on smaller supercells, the image charge and potential alignment correction terms become very large, making any errors in these terms more pronounced, potentially negating the beneficial effect of using an accurate band gap.

In order to quantify the magnitude that the calculated Br_{Se}^{0} defect formation energy must be underestimated we calculate the doping effectiveness using eqn (1) at 973 K in the Pb–PbSe–$PbBr_2$ region of Br–Pb–Se and PbSe–Na_2Se–NaSe region of Na–Pb–Se as shown in Fig. 3. In this figure, horizontal dashed lines have been used to mark the expected doping efficiencies that is known from extensive Hall effect measurements on polycrystalline PbSe doped with Br or Na to be nearly 100% for the sample $Pb_{1.002}Se_{0.992}Br_{0.008}$ and 90% for the sample $Pb_{0.9875}Na_{0.0125}Se$,[6,8,14] with the expected dominant defects being Br_{Se}^{+1} and Na_{Pb}^{-1}, respectively. These results are from samples made by first melting nominal compositions of $Pb_{1.002}Se_{1-x}Br_x$, or $Pb_{1-y}Na_ySe$. The ingots were annealed at 973 K

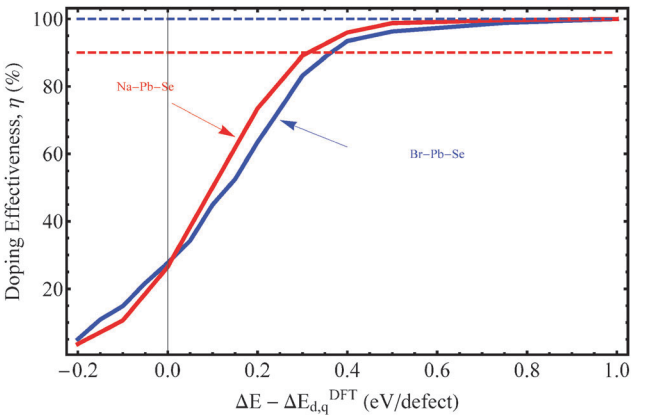

Fig. 3 Calculated doping effectiveness (computed using eqn (1)) of the shown defects at 973 K in the Pb–PbSe–$PbBr_2$ region of Br–Pb–Se and PbSe–Na_2Se–NaSe region of Na–Pb–Se calculated by varying the formation energies of the neutral Br_{Se}^{0} and Na_{Pb}^{0} defects (*x*-axis), respectively. $\Delta E - \Delta E_{d,q}^{DFT}$ indicates the change from the true DFT calculated formation energy. Dashed lines mark the experimentally measured values of doping effectiveness for each system. As can be seen from this plot, the calculated doping effectiveness in both systems matches experimental measurements only when the formation energies of the neutral defects are raised by ≈0.5 eV from the DFT value.

for 72 hours, followed by consolidation of crushed powder by hot pressing, after which their Hall effect carrier densities were measured. While Br_{Se}^{+1} produces one electron in the conduction band per Br atom, the extra 4p electron in Br_{Se}^{0} in a truly neutral defect should be localized around the defect. Thus, Br_{Se}^{0} serves only to reduce the doping effectiveness. The formation energies of the charged defects Br_{Se}^{+1} and Na_{Pb}^{-1} is expected to be as low as calculated and shown in Fig. 1 and 2 such that they dominate the defect energy landscape of the most stable defects in these systems, which indicates that it must actually be the formation energies of Br_{Se}^{0} and Na_{Pb}^{0} that must be underestimated. Upon variation of the formation energies of these neutral defects from their true DFT calculated values as shown with solid lines in Fig. 3, we find the underestimation from this plot to be at least 0.5 eV.

The severe underestimation of the Br_{Se}^{0} formation energy using DFT can be traced to delocalization of the extra Br electron in the DFT calculation, which leads us to conclude these do not represent the intended defects. Thus, in essence, this energy does not reflect the energy of the neutral defect with a localized charge, but instead the energy of a donor defect where the electron has formed a large polaronic state at the bottom of the conduction band. Such large polarons, which are essentially electrons in hydrogen atom like states around a central, charged (but screened) defect are expected from shallow defects. In Fig. 4 we plot the partial charge density of the highest occupied state calculated for PbSe with the neutral Br_{Se}^{0} defect. These electrons are clearly not localized around the Br defect but delocalized as part of the conduction band.

We also notice that the +/0 donor transition level for the Br_{Se} defect (0/− acceptor transition level in case of Na_{Pb}) is close to the CBM (VBM for Na_{Pb}), as seen in Fig. 1, consistent with these neutral defects being shallow defects. The transitions are close to the band edge because the doped electron from the Br_{Se}^{+1} defect is located in a state that looks similar to and is close in energy to the CB, as evident from Fig. 4. The calculated neutral defect Br_{Se}^{0} is thus effectively the same as the charged defect Br_{Se}^{+1} with the Fermi level located near the CBM. The defect formation energy calculated for the neutral case instead becomes correlated with the formation energy of the charged defect at the band edges. Thus, the defect energy for Br_{Se}^{0} calculated by DFT (and most likely other defects with unexpected charge states as well) does not, in fact, have the charge state intended. Instead the charge has been delocalized, altering the charge state of the defect.

Excluding the defects Br_{Se}^{0}, Na_{Pb}^{0}, and others marked with dashed lines in Fig. 1 and 2, for phase diagram calculations, we can calculate realistic isothermal sections of solvus boundaries of the PbSe phase at 973 K in the Br–Pb–Se and Na–Pb–Se ternary phase diagrams, as shown in Fig. 5 and 6, respectively. From Fig. 5 it is evident that peak Br solubility in PbSe occurs in a direction slightly Br-rich and Pb-deficient of the PbSe–PbBr line – the line for 1 : 1 substitution of Se with Br. Fig. 6 shows that the PbSe single-phase region is very narrow and has maximum Na solubility along the PbSe–NaSe line, similar to the solubility of Na predicted in PbTe in ref. 28.

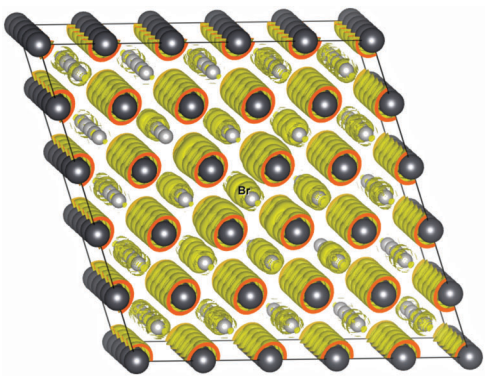

Fig. 4 Partial charge density plot of the highest energy electrons in the supercell (of the PbSe primitive cell) containing the Br_{Se}^{0} defect (at the center of the supercell) showing charge delocalization that makes this defect equivalent to the case of the charged defect Br_{Se}^{+1} with the Fermi level located at or near the CBM. Pb atoms are shown in dark grey, Se atoms in light grey, and Br atom in green.

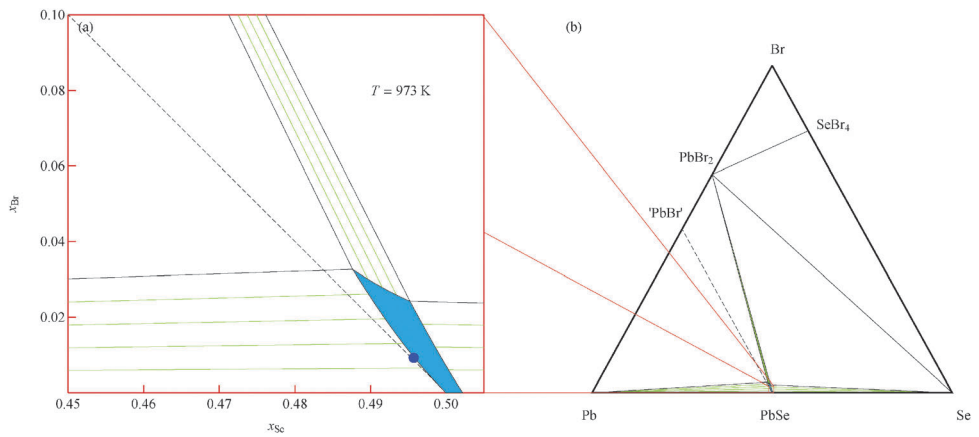

Fig. 5 (a) Isothermal section of the Br–Pb–Se phase diagram calculated at T = 973 K showing the single-phase region of PbSe in blue, and green tie-lines representing two-phase regions between it and other compounds that are shown in the full isothermal section plot in (b). Sample composition at which doping effectiveness measurements were made is shown as a closed blue circle in (a). Dashed line represents a path between PbSe and a hypothetical PbBr compound for one-to-one replacement of Se with Br, *i.e.*, as $PbBr_xSe_{1-x}$.

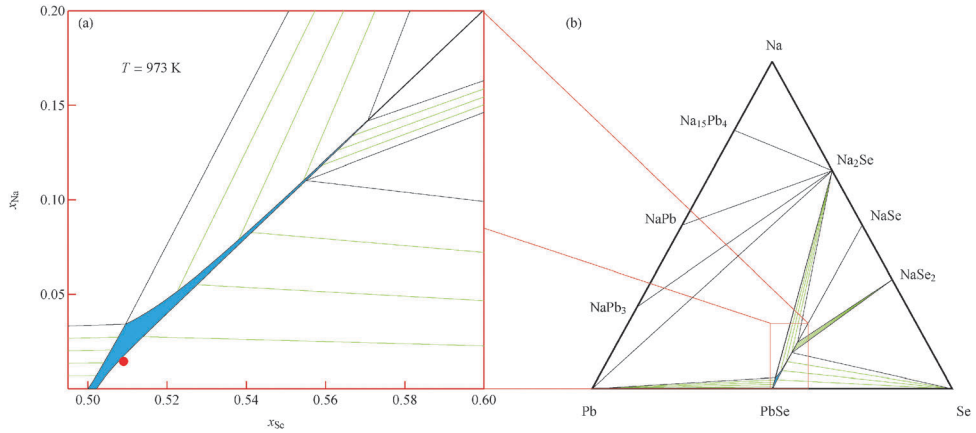

Fig. 6 (a) Isothermal section of the Na–Pb–Se phase diagram calculated at T = 973 K showing the single-phase region of PbSe in blue, and green tie-lines representing two-phase regions between it and other compounds that are shown in the full isothermal section plot in (b). Sample composition at which doping effectiveness measurements were made is shown as a closed red circle in (a).

For accurate phase diagrams and dopant effectiveness that matches experiment, we suggest using only the expected charge states for each defect (here: Br_{Se}^{+1}, Na_{Pb}^{-1}, V_{Pb}^{-2}, V_{Se}^{+2}, as marked with solid lines in Fig. 1 and 2) in calculations of phase diagrams and doping effectiveness. We suspect the problem of delocalized charge in neutral defects is widespread in calculations on easily doped, low band-gap semiconductors with high dielectric constants. Although the delocalized charge problem is understood by the defect calculation community,[39] the process of calculating defect formation energies in a system is not frequently described as a method that was primarily developed to understand deep defects in large band-gap semiconductors or insulators.

4. Conclusions

In summary, we performed standard defect energy calculations on PbSe with a n-type dopant Br and a p-type dopant Na, and found that defects with unexpected charge states result in unexpectedly low formation energies that would not agree with experimentally observed phase diagrams or dopant efficiencies. This has been traced to the delocalization of charge, which alters the charge state of the calculated defect. Thus, these defects were excluded from calculations of the phase diagrams giving results that appear accurate. Similar consideration is surely relevant to many defect calculations, particularly in narrow band gap semiconductors. Refining a procedure to identify delocalized charge and eliminating unnecessary calculations will expedite the use of such calculations by experimentalists in understanding phase diagrams and devising effective doping strategies.

Acknowledgements

This work was supported by the Department of Energys Basic Energy Sciences program – the Materials Project – under Grant No. EDCBEE. Work at Lawrence Berkeley, through discussions with Qimin Yan, Mark Asta, and Jeff Neaton, was supported by the Office of Science of the U.S. Department of Energy under Contract No. DEAC02-05CH11231. J. W. D. and C. W. acknowledge support by the U.S. Department of Energy, Office of Science, Basic Energy Sciences, under Grant DEFG02-07ER46433. The authors acknowledge the Chemical Engineering Cluster at Texas A&M University and the National Energy Research Scientific Computing Center, a DOE Office of Science User Facility supported by the Office of Science of the U.S. Department of Energy, for providing computing resources useful in conducting the research reported in this work. The figures in this article have been created using the LevelScheme scientific figure preparation system.[40]

References

1 K. Ellmer, *Nat. Photonics*, 2012, **6**, 809–817.
2 P. Hohenberg and W. Kohn, *Phys. Rev.*, 1964, **136**, B864–B871.
3 W. Kohn and L. J. Sham, *Phys. Rev.*, 1965, **140**, A1133–A1138.
4 J. Vidal, S. Lany, M. d'Avezac, A. Zunger, A. Zakutayev, J. Francis and J. Tate, *Appl. Phys. Lett.*, 2012, **100**, 032104.
5 Y. Z. Pei, X. Y. Shi, A. D. LaLonde, H. Wang, L. D. Chen and G. J. Snyder, *Nature*, 2011, **473**, 66–69.
6 H. Wang, Y. Z. Pei, A. D. LaLonde and G. J. Snyder, *Adv. Mater.*, 2011, **23**, 1366–1370.
7 L.-D. Zhao, S.-H. Lo, J. He, H. Li, K. Biswas, J. Androulakis, C.-I. Wu, T. P. Hogan, D.-Y. Chung, V. P. Dravid and M. G. Kanatzidis, *J. Am. Chem. Soc.*, 2011, **133**, 20476–20487.
8 H. Wang, Y. Z. Pei, A. D. LaLonde and G. J. Snyder, *Proc. Natl. Acad. Sci. U. S. A.*, 2012, **109**, 9705–9709.
9 G. J. Snyder and E. S. Toberer, *Nat. Mater.*, 2008, **7**, 105–114.
10 G. T. Alekseeva, E. A. Gurieva, P. P. Konstantinov, L. V. Prokofeva and M. I. Fedorov, *Semiconductors*, 1996, **30**, 1125–1127.
11 D. Parker and D. J. Singh, *Phys. Rev. B: Condens. Matter Mater. Phys.*, 2010, **82**, 035204.
12 L.-D. Zhao, S. Hao, S.-H. Lo, C.-I. Wu, X. Zhou, Y. Lee, H. Li, K. Biswas, T. P. Hogan, C. Uher, C. Wolverton, V. P. Dravid and M. G. Kanatzidis, *J. Am. Chem. Soc.*, 2013, **135**, 7364–7370.
13 H. Wang, Z. M. Gibbs, Y. Takagiwa and G. J. Snyder, *Energy Environ. Sci.*, 2014, **7**, 804–811.

14 H. Wang, X. Cao, Y. Takagiwa and G. J. Snyder, *Mater. Horiz.*, 2015, **2**, 323–329.
15 M. N. Vinogradova, I. M. Rudnik, L. M. Sysoeva and N. V. Kolomoet, *Semiconductors*, 1969, **2**, 892–893.
16 Y. Lee, S.-H. Lo, J. Androulakis, C.-I. Wu, L.-D. Zhao, D.-Y. Chung, T. P. Hogan, V. P. Dravid and M. G. Kanatzidis, *J. Am. Chem. Soc.*, 2013, **135**, 5152–5160.
17 DFT calculations in this work for the calculation of energies of the defect and host supercells are performed using VASP.[41–44] Ion–electron interactions were described using the Projector Augmented Wave (PAW) potentials[45–47] utilizing the generalized gradient approximation (GGA) with the exchange–correlation functional of Perdew, Burke, and Ernzerhof (PBE).[48] The $5d^{10}6s^{2}6p^{2}$ electrons of Pb, $4s^{2}4p^{4}$ electrons of Se, $4s^{2}4p^{5}$ electrons of Br, and $2p^{6}3s^{1}$ electrons of Na are treated as valence states in the PAW potentials. All supercell calculations are performed on a $5 \times 5 \times 5$ supercell of the primitive cell and contain 250 atoms. The cutoff energy of plane wave basis was set to 400 eV, a Gaussian smearing width of 0.1 eV is used to smear electron occupations, and integrations over the first Brillouin zone are made using a $2 \times 2 \times 2$ Monkhorst–Pack *k*-point grid.[49] Atomic positions are relaxed based on an energy convergence criteria of 10^{-4} eV without relaxing cell shape or volume in order to exclude the effect of lattice distortions on the defect energetics. A final static calculation is performed for each defect to obtain accurate total energies.
18 S. B. Zhang and J. E. Northrup, *Phys. Rev. Lett.*, 1991, **67**, 2339–2342.
19 A. Jain, S. P. Ong, G. Hautier, W. Chen, W. D. Richards, S. Dacek, S. Cholia, D. Gunter, D. Skinner, G. Ceder and K. A. Persson, *APL Mater.*, 2013, **1**, 011002.
20 S. P. Ong, L. Wang, B. Kang and G. Ceder, *Chem. Mater.*, 2008, **20**, 1798–1807.
21 A. Jain, G. Hautier, S. P. Ong, C. J. Moore, C. C. Fischer, K. A. Persson and G. Ceder, *Phys. Rev. B: Condens. Matter Mater. Phys.*, 2011, **84**, 045115.
22 S. Lany and A. Zunger, *Modell. Simul. Mater. Sci. Eng.*, 2009, **17**, 084002.
23 G. Makov and M. Payne, *Phys. Rev. B: Condens. Matter Mater. Phys.*, 1995, **51**, 4014–4022.
24 M. Gajdoš, K. Hummer, G. Kresse, J. Furthmüller and F. Bechstedt, *Phys. Rev. B: Condens. Matter Mater. Phys.*, 2006, **73**, 045112.
25 S. Baroni and R. Resta, *Phys. Rev. B: Condens. Matter Mater. Phys.*, 1986, **33**, 7017–7021.
26 X. Wu, D. Vanderbilt and D. R. Hamann, *Phys. Rev. B: Condens. Matter Mater. Phys.*, 2005, **72**, 035105.
27 L. Bjerg, G. K. H. Madsen and B. B. Iversen, *Chem. Mater.*, 2012, **24**, 2111–2116.
28 J. W. Doak, K. J. Michel and C. Wolverton, *J. Mater. Chem. C*, 2015, **3**, 10630–10649.
29 S. Bajaj, H. Wang, G. J. Snyder, unpublished.
30 Y. Takagiwa, Y. Pei, G. Pomrehn and G. J. Snyder, *Appl. Phys. Lett.*, 2012, **101**, 092102.
31 Y. Takagiwa, Y. Pei, G. Pomrehn and G. J. Snyder, *Appl. Phys. Lett.*, 2013, **1**, 011101.
32 S. Lany and A. Zunger, *Phys. Rev. B: Condens. Matter Mater. Phys.*, 2008, **78**, 235104.
33 Z. M. Gibbs, H. Kim, H. Wang, R. L. White, F. Drymiotis, M. Kaviany and G. J. Snyder, *Appl. Phys. Lett.*, 2013, **103**, 262109.
34 *Semiconductors: Group IV Elements, IV-IV and III-IV Compounds, Landolt-Börnstein, New Series, Group III, Vol. 41, Pt. A*, ed. O. Madelung, U. Rössler and M. Schulz, Springer-Verlag, Berlin, 2005.
35 W. H. Strehlow and E. L. Cook, *J. Phys. Chem. Ref. Data*, 1973, **2**, 163–199.
36 K. Hummer, A. Grüneis and G. Kresse, *Phys. Rev. B: Condens. Matter Mater. Phys.*, 2007, **75**, 195211.
37 Y. Zhang, X. Ke, C. Chen, J. Yang and P. R. C. Kent, *Phys. Rev. B: Condens. Matter Mater. Phys.*, 2009, **80**, 024304.
38 A. Svane, N. E. Christensen, M. Cardona, A. N. Chantis, M. van Schilfgaarde and T. Kotani, *Phys. Rev. B: Condens. Matter Mater. Phys.*, 2010, **81**, 245120.
39 C. Freysoldt, B. Grabowski, T. Hickel, J. Neugebauer, G. Kresse, A. Janotti and C. G. Van de Walle, *Rev. Mod. Phys.*, 2014, **86**, 253–305.
40 M. A. Caprio, *Comput. Phys. Commun.*, 2005, **171**, 107–118.
41 G. Kresse and J. Hafner, *Phys. Rev. B: Condens. Matter Mater. Phys.*, 1993, **47**, 558–561.
42 G. Kresse and J. Hafner, *Phys. Rev. B: Condens. Matter Mater. Phys.*, 1994, **49**, 14251–14269.
43 G. Kresse and J. Furthmüller, *Comput. Mater. Sci.*, 1996, **6**, 15–50.
44 G. Kresse and J. Furthmüller, *Phys. Rev. B: Condens. Matter Mater. Phys.*, 1996, **54**, 11169–11186.
45 P. E. Blöchl, *Phys. Rev. B: Condens. Matter Mater. Phys.*, 1994, **50**, 17953–17979.
46 G. Kresse and D. Joubert, *Phys. Rev. B: Condens. Matter Mater. Phys.*, 1999, **59**, 1758–1775.
47 O. Bengone, M. Alouani, P. Blöchl and J. Hugel, *Phys. Rev. B: Condens. Matter Mater. Phys.*, 2000, **62**, 16392–16401.
48 J. P. Perdew, K. Burke and M. Ernzerhof, *Phys. Rev. Lett.*, 1996, **77**, 3865–3868.
49 H. J. Monkhorst and J. D. Pack, *Phys. Rev. B: Solid State*, 1976, **13**, 5188–5192.